New Journal of Physics
The open access journal at the forefront of physics

Deutsche Physikalische Gesellschaft DPG
IOP Institute of Physics

Published in partnership with: Deutsche Physikalische Gesellschaft and the Institute of Physics

OPEN ACCESS

RECEIVED
9 December 2021

REVISED
6 June 2022

ACCEPTED FOR PUBLICATION
18 July 2022

PUBLISHED
10 August 2022

PAPER

Multi-GeV cascaded laser wakefield acceleration in a hybrid capillary discharge waveguide

Zhiyong Qin[1,2], Wentao Li[3,*], Jiaqi Liu[1], Jiansheng Liu[2,*], Wentao Wang[1], Changhai Yu[2], Zhijun Zhang[2], Xinliang Wang[1], Jinfeng Li[1], Yuxin Leng[1], Xiaoyan Liang[1], Ruxin Li[1,*] and Zhizhan Xu[1,*]

[1] State Key Laboratory of High Field Laser Physics and CAS Center for Excellence in Ultra-intense Laser Science, Shanghai Institute of Optics and Fine Mechanics, Chinese Academy of Sciences, Shanghai 201800, People's Republic of China
[2] Department of Physics, Shanghai Normal University, Shanghai 200234, People's Republic of China
[3] SUPA, Department of Physics, University of Strathclyde, Glasgow G4 0NG, United Kingdom
[*] Authors to whom any correspondence should be addressed.

E-mail: wentao.li@strath.ac.uk, liujs@shnu.edu.cn, ruxinli@mail.shcnc.ac.cn and zzxu@mail.shcnc.ac.cn

Keywords: laser wakefield acceleration, capillary discharge waveguide, ionization-induced injection, high-energy electron beams, particle-in-cell-simulations

Abstract

Based on a 6 cm-long two-segment hybrid capillary discharge waveguide, a multi-GeV electron beam with energy up to 3.2 GeV and 9.7% rms energy spread was achieved in a cascaded laser wakefield acceleration scheme, powered by an on-target 210 TW laser pulse. The electron beam was trapped in the first segment via ionization-induced injection, and then seeded into the second segment for further acceleration. The long-distance stable guiding of the laser pulse and suppression of the dark current inside the second-segment capillary played an important role in the generation of high-energy electron beams, as demonstrated by quasi-three-dimensional particle-in-cell simulations.

1. Introduction

Laser wakefield accelerators (LWFAs) provide a large acceleration gradient on the order of tens to hundreds of GV m^{-1} [1–3], making them attractive acceleration schemes for producing 10 GeV or even 100 GeV-scale electron beams on a compact scale [4–6]. Over the past decades, great progress has been made in LWFAs [7–10], yielding high-energy electron beams (*e* beams) with multi-GeV [11–15] and high-quality *e* beams [16–22] with monoenergetic, high-brightness, and low-emittance, leading to a variety of applications in coherent x-ray sources, gamma-ray sources and free electron lasers [23–28].

Although GeV *e* beams have been produced with petawatt laser systems in self-guided plasmas [12, 13, 29], the best way to boost the *e*-beam energy to multi-GeV or more is to use preformed plasma waveguides. Similar to graded-index optical fibers, a parabolic plasma channel with an axis minimum in the electron density can be used to guide laser pulses over a long distance when the laser spot size equals the matched spot size of the channel [3], which can increase the acceleration length and energy gain of *e* beams for a certain laser power [30, 31]. In general, the performed plasma channel is formed by a gas-filled [32–34] or ablative [35–37] capillary discharge waveguide (CDW) and has been demonstrated in LWFA experiments [11, 14, 15, 38, 39]. Although both types of CDWs can generate plasma channels, the process of channel formation is not exactly the same owing to their different plasma sources. In gas-filled CDW, the plasma mainly originates from the ionization of the prefilled gas during discharge. After breakdown, the discharge current begins to heat and ionize the prefilled gas, increasing the plasma temperature. After full ionization, the plasma is in quasi-steady-state equilibrium, which gives a plasma temperature profile with its maximum on the axis and minimum on the wall owing to the balance of ohmic heating and thermal conduction to the cold capillary wall. As the plasma pressure is radially uniform, this monotonic radially decreasing temperature results in an axial minimum plasma density profile, which is the plasma channel

[40, 41]. In ablative CDW, plasma mainly originates from the ablation and ionization of the inner capillary wall. After breakdown, the inner wall begins to ablate and vaporize, and the plasma temperature begins to increase as the discharge current increases. Further, the ablated and evaporated plasma begins to ionize, with the fast plasma compression occurring from the periphery to the axis. With the balance between ohmic heating and thermal conduction to the cold capillary wall, the plasma temperature has its maximum on the axis and minimum on the capillary wall, which also leads to the formation of a plasma channel with an axial minimum the plasma density [35, 40, 42]. Compared with the ablative CDW, the gas-filled CDW has a higher discharge stability and longer lifetime [34] and is often used in LWFA to achieve multi-GeV *e* beams. Recently, a sapphire machined gas-filled CDW was used in LWFA experiments to guide laser pulses over a distance of 20 cm, *e* beams with energy approaching 10 GeV were obtained with a petawatt-class laser [15]. However, owing to its complicated manufacturing processes, it is difficult to make the gas-filled CDWs longer in a single piece or stick multiple CDWs together without any gas leakage and deformation [43], which is very important for higher energy acceleration and cascaded acceleration.

Compared with the gas-filled CDW, the ablative CDW has rarely been used in LWFA experiments [35, 38, 39] in the past few decades because of its poor discharge stability and short lifetime. The limited lifetime and poor discharge ability can be attributed to the adsorbed gas exhaustion and inner-wall erosion during discharge [37, 44]. In such an ablative CDW, the discharge is triggered by the ionization of the adsorbed gas in the inner wall and is dominated by the ablation and evaporation of the inner wall. After some repeated discharge processes, the inner wall of the capillary would become smooth and the adsorbed gas would also get exhausted, resulting in a short lifetime and poor discharge stability with dramatic jitter. Nevertheless, the bulk material of ablative CDWs is polyethylene (PE) $[(C_2H_4)_n]$ or acrylic resin (AR) $[(C_3H_4O_2)_n]$, which is cheaper, easily mechanically machinable, and can be made longer in length in a single piece or easily stuck together without considering gas leakage. In view of the disadvantages of ablative CDWs, in reference [37], we have demonstrated a hybrid CDW by filling a pure ablative capillary with a low-pressure gas (3.8 Torr). In the hybrid CDW, the prefilled gas is just used to replace the adsorbed gas and acts as the seed plasma to trigger the discharge process. The plasma still mainly comes from the wall ablation, which is the same as purely ablative CDW. By using this hybrid CDW, the discharge stability and lifetime can be greatly improved, which provides an effective way for 10 GeV or even 100 GeV-scale *e* beams generation in LWFAs [4, 45].

In this paper, multi-GeV *e* beams with peak energy up to 3.2 GeV, 9.7% rms energy spread, 1.45 pC electron charge, and ∼1.4 mrad rms divergence are experimentally produced from a cascaded LWFA based on a two-segment (2 cm + 4 cm) hybrid CDW. The experimental results suggest that this was achieved via ionization-induced injection of oxygen K-shell electrons from the ablation of the oxygen-containing AR capillary wall. Quasi-three-dimensional particle-in-cell (quasi-3D PIC) simulations support the experimental results and further reveal good optical guiding of the driving laser pulse and a dark-current-free acceleration process that contributed dominantly to the *e*-beam high energy gain.

2. Experimental results

2.1. Experimental setup

The experiments were carried out at the petawatt laser facility at the SIOM. The experimental setup is shown in figure 1, where an 800 nm laser pulse with a full width at half maximum pulse duration of 50 fs was focused at the entrance of the hybrid CDW by a $f/30$ off-axis parabolic mirror. The focal spot size w_0 was measured to be 46 ± 1.0 μm at $1/e^2$ of the peak intensity, as shown in figure 1(a), its Strehl ratio was optimized to be 0.8 with a deformable mirror and a wave-front sensor. With an on-target peak power of 210 TW, the laser peak intensity was estimated to be 6.1×10^{18} W cm^{-2}, corresponding to a normalized amplitude of $a_0 = 1.65 \pm 0.1$. The hybrid CDW is shown in figure 1(b), where single-segment (2 cm) and two-segment (2 cm + 4 cm) capillaries are used in the experiments. The capillary bulk material was AR or PE and low-pressure hydrogen gas or mixture gas (3.8 Torr) was supplied to it to provide the seed plasma for discharge breakdown [37]. The inner diameter of the hybrid capillary was 500 μm and the applied discharge voltage was 22–25 kV with a maximum discharge current from 90–110 A.

The main laser pulse was focused to propagate through the capillary axially, reflected by a 100 μm-thick titanium foil and then dumped to protect the 300 μm-thick beryllium window on the vacuum chamber. The generated *e* beams were dispersed by a 76 cm-long magnetic spectrometer with a magnetic field of 1.3 T. A removable 15 cm-long collimator with a hole of 5 mm in diameter was placed in front of the magnetic spectrometer to block large-divergence x-rays and peripheral low-energy electrons. As shown in figure 1, the *e* beams were imaged by downstream imaging plates (IPs, Fujifilm BAS-IP SR 2040 E, 50 μm pixels), and the signals were detected by a Fuji-labeled FLA-7000 IP scanner for the photo-stimulated

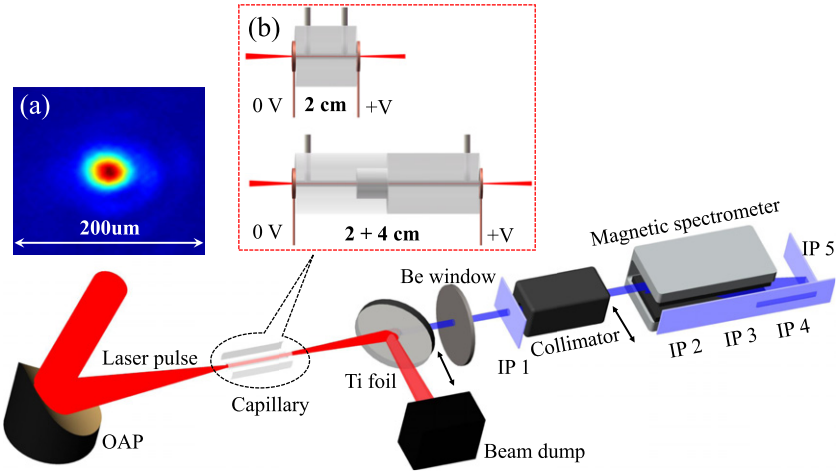

Figure 1. Experimental setup for the cascaded LWFA. (a) Measured laser focal spot. (b) Structures of the single-segment and two-segment hybrid capillaries.

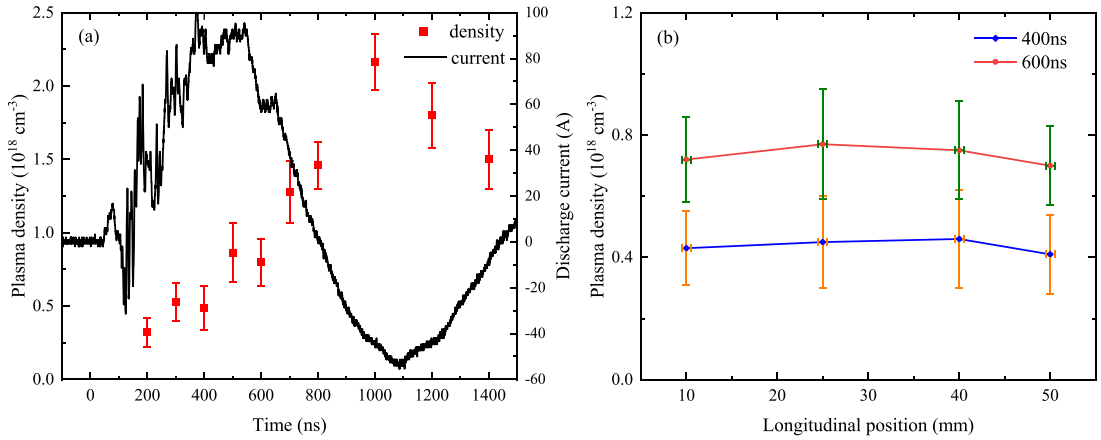

Figure 2. Measured plasma densities in the two-segment (2 cm + 4 cm) hybrid CDW with 3.8 Torr hydrogen gas and 24.5 kV discharge voltage. (a) Temporal evolution of the on-axis plasma density and the discharge current. (b) Longitudinal plasma density profile at different time delays. The error bar at each point represented 15 repeated measurements in three identical hybrid CDWs (five repeated measurements in each capillary).

luminescence (PSL) levels, which were then converted into the electron beam charge with the published sensitivity (PSL/electron) [46].

2.2. Plasma density measurement

The plasma density was measured by investigating the Stark broadening of the H_α line using a spectrometer (1200 lines mm^{-1} grating) equipped with an intensified charge-coupled device (ICCD, Andor iStar 303i). By measuring the emitted H_α spectrum during discharge in the longitudinal and transverse directions, the plasma density in the capillary can be obtained [37, 47], as shown in figure 2. Figure 2(a) shows the temporal evolution of the on-axis plasma density and discharge current in a two-segment (2 cm + 4 cm) hybrid CDW. It can be seen that the plasma density increased with the discharge current until it reached its maximum, which was in agreement with the simulation [35]. The on-axis plasma density was about 0.7×10^{18}–1.2×10^{18} cm^{-3} within the plasma channel temporal window [37]. To determine the longitudinal plasma density profile, a transverse single-point method, as described in reference [47], was used to collect the discharge spectrum and measure the plasma density at different longitudinal positions (10, 25, 40, and 50 mm) along the axis and different time delays (400 and 600 ns). The results were shown in figure 2(b), where the average plasma density at the moment of 400 and 600 ns was 0.44×10^{18} and 0.75×10^{18} cm^{-3}, and the longitudinal plasma density variation was about 6.8% and 6.6% of their average value, respectively.

Compared to the transverse interferometry method [32], the single-point spectrum method used in our experiments to measure the plasma density had some limitations. First, this method could make only single point measurement in a single discharge shot and unable to measure the overall longitudinal plasma density

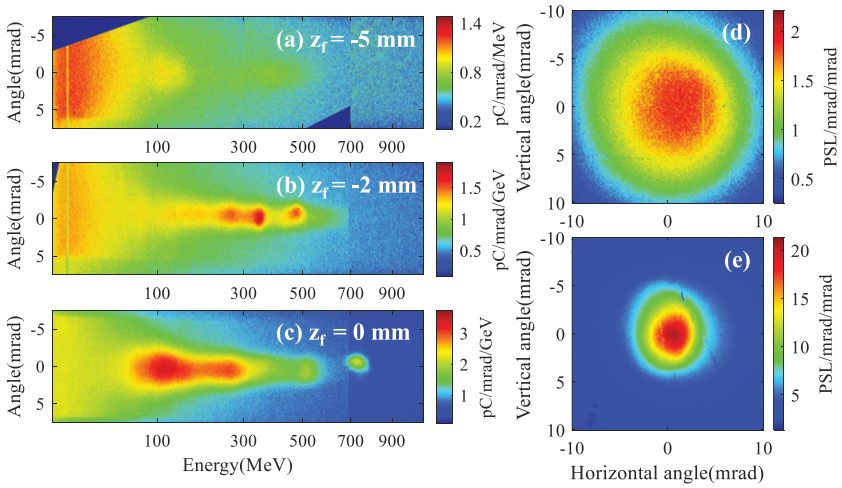

Figure 3. Typical energy spectra of the generated *e* beams in different focal positions. (a) $z_f = -5$ mm, (b) $z_f = -2$ mm, (c) $z_f = 0$ mm. The *e*-beam spatial distributions at $z_f = -5$ mm and $z_f = 0$ mm are shown in (d) and (e) with corresponding divergence angles of 14 and 6 mrad, respectively.

profile in a single shot. In addition, the jitter of each discharge shot may also cause errors in plasma density measurement in our ablative hybrid CDW. Second, the emitted H_α spectrum during discharge was susceptible to self-absorption in dense plasma ($n_e > 10^{18}$ cm^{-3}), which may lead to an over-estimation of the plasma density [48]. Finally, the intensity of the discharge spectrum collected in transverse direction was very weak, which reduced the resolution of the spectrometer and also led to the large error bars in figure 2(b). Nevertheless, the average plasma densities of the measured four points along the capillary were very close, which was in agreement with previous simulation and experimental results [42, 49, 50].

2.3. LWFA with a single-segment CDW

First, a single-segment (2 cm) hybrid capillary made of AR was used in the experiments. Low-pressure hydrogen gas at 3.8 Torr was injected into the capillary to maintain the discharge stability, and the applied discharge voltage was 22 kV. The driving laser pulse arrived ~600 ns after discharge, which was just in the time window of the preformed plasma channel [37], and the corresponding plasma density was about 7.5×10^{17} cm^{-3}, as shown in figure 2. Three typical shots of the *e*-beam spectra at different focal positions, as shown in figure 3, demonstrated that the accelerated *e* beams could be controlled by adjusting the laser focus. When the focal position was 7 mm outside the capillary entrance ($z_f = -7$ mm), few electrons were detected in the experiments, indicating that the laser pulse was not well coupled into the discharge capillary in this case. By shortening the focal position to $z_f = -5$ mm, two *e* beams were observed, as shown in figure 3(a). The first *e*-beam energy was lower than 200 MeV with electron charge of 0.7 pC, and the second *e* beam just with smaller charge of 0.2 pC were accelerated further to 500 MeV. When the focal position was further changed to $z_f = -2$ mm, several *e* beams were observed as shown in figure 3(b). The maximum peak *e*-beam energy was about 500 MeV and the electron charge increased to 1.54 pC. Moreover, when the focal position was located at the capillary entrance ($z_f = 0$ mm), an *e* beam with a peak energy up to 0.73 GeV, 6.8% rms energy spread, 1.4 pC charge and 1.0 mrad rms divergence was obtained, as shown in figure 3(c). The IP in front of the magnetic spectrometer was used to detect the spatial profiles of the whole generated *e* beams. Figures 3(d) and (e) show the *e*-beam spatial profiles at $z_f = -5$ mm and $z_f = 0$ mm, where the corresponding *e*-beam divergence angles were 14 mrad and 6 mrad, respectively. It can be seen that the *e*-beam transverse oscillation at $z_f = -5$ mm was stronger than that at $z_f = 0$ mm, which can be attributed to a poor guidance of the laser pulse at $z_f = -5$ mm. The significant oscillation in laser spot size would lead to a significant oscillation of the bubble size, which can further lead to an enhanced *e*-beam transverse oscillation and a large divergence angle [51–54]. Therefore, compared with the cases of $z_f = -5$ mm and $z_f = -2$ mm, the driving laser pulse was well guided in the capillary when the laser focus was located at $z_f = 0$ mm.

We have demonstrated that although low-pressure hydrogen gas was supplied, the plasma generated during the discharge mainly came from the ablation of the inner wall of the hybrid capillary [37]. Moreover, as shown in our previous work, assisted by oxygen, ionization-induced injection can occur in an AR capillary [39]. In the experiments, by moving the focal position from $z_f = -5$ mm to $z_f = 0$ mm, more laser pulse energy can be coupled into the capillary, leading to a gradually enhanced self-focusing. Once the laser

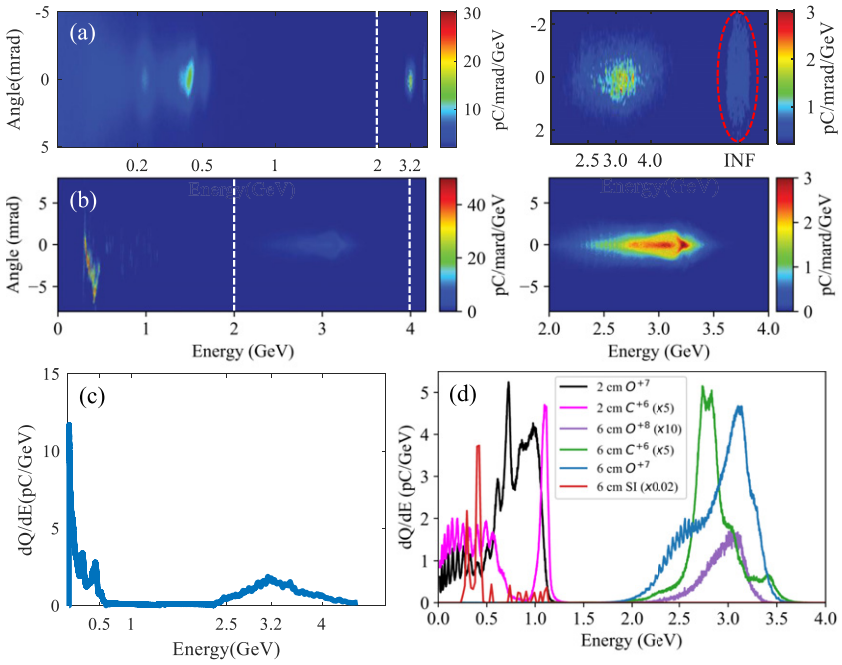

Figure 4. Energy spectra obtained from two-segment hybrid capillary: (a) experimental results with 3.8 Torr H_2 filled gas; (b) simulated results by FBPIC code. The right-hand column corresponds the white dashed region in (a) and (b), which shows the detailed spectrum of the high energy *e* beams. The area circled by a dashed red line in (a) is the detected x-ray passing through the collimator. The detailed angle-resolved energy spectrum corresponding to (a) and (b) are shown in (c) and (d), respectively. The plots in (d) were final energy spectrum of electrons from O^{+7} (blue), O^{+8} (purple), C^{+6} (green) and SI (red), and energy spectrum of electrons from O^{+7} (black) and C^{+6} (pink) at $z = 2$ cm. The peak energy of the multi-GeV *e* beam observed in experiments was 3.2 GeV, and the simulated *e*-beam peak energy was about 3.1 GeV.

pulse is self-focused with intensity exceeding the threshold for generating O^{7+} ($a > 2.9$), electron injection can be induced by tunneling ionization. It is worth noting that a low energy spread *e* beam with 0.73 GeV peak energy was observed in the experiments (figure 3(c)), which means that the *e* beam was injected later and should still be in an early acceleration phase in the wake at the end of the capillary. Besides, the injected electron charge of the *e* beam was only about 1.4 pC, indicating that the laser pulse was not strongly self-focused, and the injection process only lasted for a short time.

2.4. Cascaded LWFA with a two-segment CDW

In order to further increase the *e*-beam energy, a cascaded LWFA with a two-segment (2 cm + 4 cm) hybrid capillary was also used in the experiments, as shown in figure 1(b). A 2 cm-long oxygen-containing AR capillary was used as the first segment to generate the seed *e* beam, and a second segment capillary (4 cm) was used as the acceleration stage in the experiments. The second segment capillary was made of PE, which is an oxygen-free material that was used to suppress subsequent ionization-induced injection. The two-segment hybrid capillary was filled with 3.8 Torr H_2 and the applied voltage was increased to 24.5 kV to maintain the same discharge current and plasma density. The focal position of the driving laser was $z_f = 0$ mm, and the experimental results are shown in figures 4(a) and (c). In figure 4(a), the entire measured *e*-beam energy spectrum is shown on the left, and a high-energy subset from the same shot is shown on the right. Figure 4(c) shows the corresponding *e*-beam angle-integrated energy spectrum, where the peak energy of the multi-GeV *e* beam was 3.2 GeV with 9.7% rms energy spread, 1.4 mrad rms divergence and 1.45 pC electron charge. The uncertainty of the peak energy was estimated to be about $\pm$ 0.2 GeV. It can be seen that the mean acceleration field was estimated to be about 53.3 GeV m^{-1}, which is higher than that obtained in references [14, 15]. The measured charge of the 3.2 GeV *e* beam was roughly equal to that of the 0.73 GeV *e* beam in figure 3(c), indicating that this high-energy *e* beam mainly originated from the ionization-induced injection in the first-segment capillary and was further accelerated in the second segment.

Several factors may contribute to the high energy in our scheme. First, as mentioned above, the *e* beam injected in the first stage was far from dephasing when seeded into the second stage and could thus be accelerated for a long distance in the second stage. Second, owing to the intensity dependence of the nonlinear plasma wavelength, the evolution of the laser intensity during the propagation process may optimize the beam phase in the wake and enhance the energy gain. Finally, no *e* beam was observed

between 0.5 GeV and 2.5 GeV in figure 4(a), which means that there was no continuous electron injection in the second stage. The *e* beam with energy lower than 0.5 GeV in figure 4(a) may come from the self-injection (SI) at the end of the second-segment capillary, which could not affect the acceleration process of the high-energy *e* beam. Therefore, the dark current was significantly suppressed by using an oxygen-free material in the second-segment hybrid capillary. With the free dark current and small charge (1.45 pC) of the *e* beam, the beam loading effect is insignificant, which might be the main reason for the high energy gain in the second stage.

3. Particle-in-cell simulations

Quasi-3D PIC simulations were performed with FBPIC code [55] to explain the electron injection and high-energy gain for the cascaded LWFA in an 6 cm-long two-segment hybrid CDW. The laser parameters used in the simulations matched with the experimental conditions. The simulations were run with a moving window, where the box sizes in longitudinal and radial directions were 80 and 150 μm with a resolution of $\Delta z = 0.033$ μm and $\Delta r = 0.15$ μm, respectively. The simulations were carried out by Lorentz-boosted frame technique [56] with $\gamma_{boost} = 5$. The incident linearly polarized laser pulse had a wavelength of 0.8 μm, focal spot size $w_0 = 45$ μm, pulse duration 50 fs, and a normalized potential vector $a_0 = 1.6$. The simulation results are shown in figures 4 and 5, where figures 4(b) and (d) show the simulated *e*-beam energy spectra. It can be seen that an *e* beam with peak energy of about 3.1 GeV, 5.9% rms energy spread and 2.1 pC charge was obtained in the simulation, as shown in right-hand column of figure 4(b) and blue plot in figure 4(d), which was consistent with the experimental results. In the simulation, the longitudinal plasma density was approximated to a trapezoidal profile [14, 15, 50], as shown in figure 5(a) by the blue curve, where its plateau density is $n_e = 0.75 \times 10^{18}$ cm^{-3}. The evolution of the transverse laser intensity along the propagation direction is shown in figure 5(a), and it can be seen that the laser pulse was well guided in the plasma channel. With the self-focusing of the laser pulse, the wake gradually evolved from a quasilinear regime to a nonlinear bubble regime. After a propagation distance of $z \approx 1$ cm, the peak normalized laser vector (red curve) reached its first maximum, $a_0 \approx 3.0$, exceeding the tunneling ionization threshold for generating O^{7+} and triggering the ionization-induced injection of oxygen K-shell electrons, as shown in figure 5(b). Subsequently, the laser intensity dropped to a local minimum of $a_0 \approx 2.4$ at about $z = 1.5$ cm, leading to a rephasing of the injected *e* beams in the wakefield owing to the intensity dependence of the nonlinear plasma wavelength. Therefore, at the end of the first-segment capillary ($z \approx 2$ cm), the *e* beam was still at the rear of the wakefield, as shown in figure 5(c). After that, the laser pulse amplitude oscillated weakly at a long propagation distance ($\sim$2.0 cm) and the bubble size remained almost unchanged, which contributed to a steady acceleration process of the *e* beam in the wakefield and its energy increased significantly, as shown in figure 5(d). For $z > 4.0$ cm, as shown in figure 5(e), because of self-steepening, the laser intensity increased significantly again, which led to an expansion of the bubble size and fast dephasing of the *e* beam. In this region, owing to the increase in laser intensity, the electrons from the second-segment capillary were self-injected into the wake at $z = 5.7$ cm, as shown in figure 5(e). Nevertheless, this self-injected *e* beam did not affect the acceleration of the high-energy *e* beam. Therefore, as previously mentioned, the hybrid CDW confined the laser pulse over a long distance and significantly increased the *e*-beam dephasing length, which contributed to a high energy gain. In addition, it can be seen from figures 5(b)–(e) that there was no additional electron injection in the second-segment capillary, except for the self-injected *e* beam at the end of the second-segment capillary, so the dark current was greatly suppressed. Moreover, because of the lower charge of the high-energy *e* beam, the beam-loading effect was not observed in the simulation. All these factors also contributed to the generation of this high-energy *e* beam.

Further investigation of the simulations showed that the high-energy *e* beams mainly came from the ionization-induced injection of $O^{+6} \rightarrow O^{+7}$ in the first segment capillary, but very few came from $O^{+7} \rightarrow O^{+8}$ and $C^{+5} \rightarrow C^{+6}$, as shown in figures 5(f)–(h). This was because the laser pulse intensity during the self-focusing process far exceeded the ionization threshold for generating C^{+6} ($a > 1.6$) but was lower than the ionization threshold for generating O^{+8} ($a > 3.5$). The C^{+6} electrons can be ionized completely by the very front of the laser pulse and are almost impossible to inject. The angle-resolved energy spectra of the electrons from O^{+7} (black and blue curves), O^{+8} (purple curve), and C^{+6} (pink and green curves) at $z =$ 2 cm (single-segment capillary) and $z = 6$ cm (two-segment capillary) are shown in figure 4(d). The *e*-beam peak energy of the O^{+7} at the end of the first segment (black curve in figure 4(d)) was about 0.73 GeV with 25.2% rms energy spread and a charge of 2.3 pC, indicating that the energy spread and electron charge in simulations was larger than the experimental results. This can be attributed to the overestimation of ionization-induced injection in the simulations [57]. Despite this minor difference, the simulation results agree well with the experimental results. Because the second-segment capillary was made

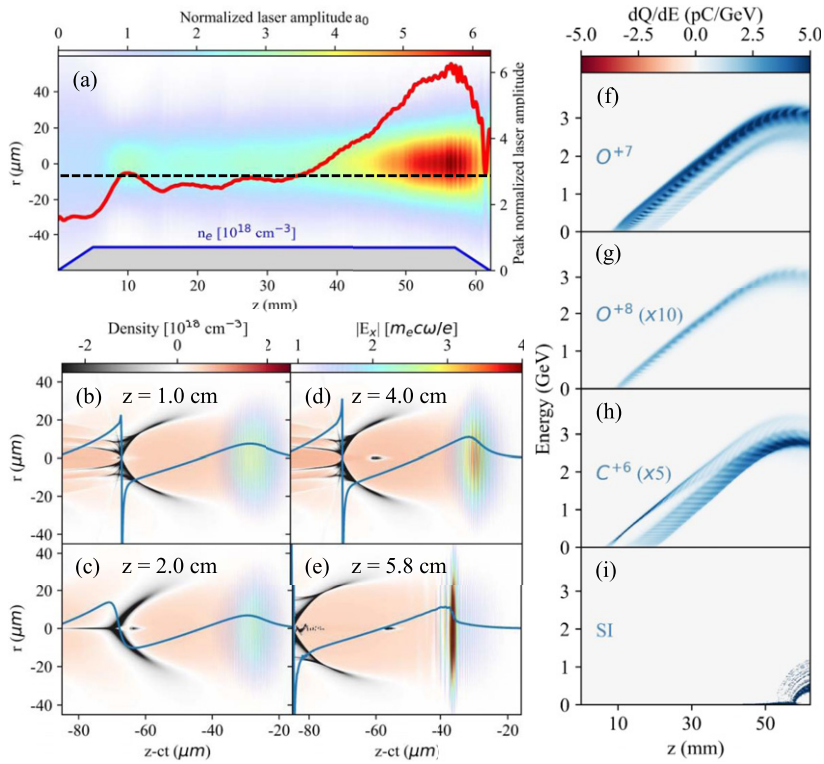

Figure 5. PIC simulation results for LWFA based on a two-segment hybrid capillary. (a) Evolution of transverse normalized laser amplitude, the corresponding peak value (red) and longitudinal plasma density distribution (blue) with a plateau density of $n_e = 0.75 \times 10^{18}$ cm^{-3} used in the simulations, the dashed black line denotes the threshold for generating O^{+7} ($a = 2.9$). (b)–(e) The snapshots of wakefield (electron density distribution) and corresponding longitudinal acceleration field (blue) at different longitudinal locations. (f)–(i) The energy evolutions of *e* beams from O^{+7}, O^{+8}, C^{+6} and SI along the propagation.

of an oxygen-free material, it could suppress continuous ionization-induced injection during the acceleration stage. As in the experiment, there was no additional electron injection in the second-segment capillary except for the later self-injected electrons in the simulation, therefore, the dark current was greatly suppressed. The energy evolution and energy spectrum of the later self-injected *e* beam are shown in figures 5(i) and 4(d) (red) with a peak energy of about 0.41 GeV, corresponding to the low-energy *e* beam observed in the experiments (low-energy parts in figure 4(a)). Therefore, because of a well-guided laser pulse and free dark current, the generated *e* beam from the first segment could be further accelerated in the second-segment capillary to high energy. The peak energy of the high-energy *e* beam was about 3.1 GeV with an 5.9% rms energy spread and a 2.1 pC electron charge, which is in good agreement with the experimental results.

4. Discussion and conclusion

In this work, high-energy *e* beams were obtained in a two-segment hybrid CDW via ionization-induced injection of partially ionized plasmas from wall ablation. It is worth mentioning that although ionization-induced injection from the wall ablation has already been proposed in a sapphire-machined CDW in 2008 [58], the CDW used in that work was still essentially a gas-filled one because its plasma mainly came from the ionization of the prefilled gas, which is different to our hybrid CDW. In our hybrid CDW, the filled low-pressure gas (3.8 Torr H_2) was only used as the seed plasma to trigger the discharge process, and the plasma mainly came from wall ablation, which was essentially an ablative CDW. Therefore, compared with the work in 2008 [58], the ionization-induced injection from capillary wall ablation is easier to realize in the ablative CDW and our hybrid CDW because of the lower melting temperature of the bulk material [39]. However, the laser damage and accumulated ablation of the wall may lead to an increase of the inner wall radius, wall deformation and blistering, which will lead to discharge instability and discharge current shape deformation after some repeated discharge processes [35, 37]. By measuring the discharge time delay and discharge current shape, the lifetime of our hybrid CDW was estimated to be over 200 shots, but about 30 shots for a pure ablative capillary [37]. Therefore, compared with the gas-filled CDW [34], both the pure ablative CDW and the hybrid CDW has a limited lifetime and cannot operate at high repetition rates at present. Nevertheless, considering the cost of installation and ease of operation, the

drawbacks of the hybrid CDW and pure ablative CDW are tolerable. Moreover, the lifetime of our hybrid CDW is longer than that of the pure ablative CDW and more suitable for high energy LWFA experiments with a low repetition rate.

Although the mean acceleration field obtained in our two-segment hybrid CDW was higher than that obtained in references [14, 15], the *e* beams in our experiments had a significantly lower charge and higher energy spread, which should be improved in future. Because the bulk material of our hybrid capillary is easily ablative, mechanically machinable, and can be joined together by several segments made of different materials, it can help us to improve the *e*-beam quality in future LWFA experiments. On one hand, by adding a small piece of oxygen-containing segment (e.g., AR) between two oxygen-free segments (e.g., PE) and sticking them together to form a hybrid CDW, the duration of the ionization-induced injection of oxygen K-shell electrons can be greatly reduced, which can decrease the *e*-beams energy spread. By changing the location and length of the small piece of the oxygen-containing segment, multi-GeV *e* beams with a lower energy spread can be obtained. On the other hand, by increasing the applied voltage, the ablation of the capillary wall can be significantly enhanced to increase the plasma density, which would result in higher charge *e* beams. In addition, by changing the filled low-pressure gas composition from pure H_2 to a mixture gas (e.g., 95% H_2 + 5% N_2), *e*-beams from the hybrid capillary can also be achieved by ionization-induced injection of the prefilled gas mixture, which can also increase the *e*-beams charge. Therefore, by changing the bulk material, length, prefilled gas, and applied voltage of the hybrid CDW, the generated *e*-beams peak energy, charge and energy spread can be controlled. This is expected to produce high-quality *e* beams with high charge and low energy spread in future.

In conclusion, a hybrid CDW was demonstrated to obtain multi-GeV *e* beams in cascaded LWFA experiments. The hybrid capillary used in our experiments combines the advantages of a pure ablative capillary and gas-filled capillary, which can not only be easily extended to a longer length in a single piece or by adding multiple segments, but also has a stable discharge process and a long lifetime. All the advantages of the hybrid capillary are very attractive for high-energy LWFA. By using a two-segment (2 cm + 4 cm) hybrid discharge capillary, a multi-GeV *e* beam with a peak energy of up to 3.2 GeV and energy spread of 9.7% was obtained in a cascaded LWFA, which demonstrates the great potential of the hybrid CDW for the generation of much higher energy *e* beams beyond 10 GeV in LWFA in the coming years.

Acknowledgments

This work was supported by the National Natural Science Foundation of China (Grants Nos. 11974251, 12105180, 11904377, 11905279, 11127901, 11875065, and 11991072), the Innovation Program of Shanghai Municipal Education Commission (Grant No. 2021-01-07-00-02-E00118), the Strategic Priority Research Program (B) (Grant No. XDB16), the State Key Laboratory Program of the Chinese Ministry of Science and Technology, and financial support from the Youth Innovation Promotion Association, CAS (Y201952).

Data availability statement

The data that support the findings of this study are available upon reasonable request from the authors.

ORCID iDs

Zhiyong Qin https://orcid.org/0000-0003-0208-8109
Jiaqi Liu https://orcid.org/0000-0002-7112-9691

References

[1] Tajima T and Dawson J M 1979 Laser electron accelerator *Phys. Rev. Lett.* **43** 267
[2] Malka V, Faure J, Gauduel Y A, Lefebvre E, Rousse A and Phuoc K T 2008 Principles and applications of compact laser–plasma accelerators *Nat. Phys.* **4** 447
[3] Esarey E, Schroeder C B and Leemans W P 2009 Physics of laser-driven plasma-based electron accelerators *Rev. Mod. Phys.* **81** 1229
[4] Nakajima K, Kim H T, Jeong T M and Nam C H 2015 Scaling and design of high-energy laser plasma electron acceleration *High Power Laser Sci. Eng.* **3** e10
[5] Debus A, Pausch R, Huebl A, Steiniger K, Widera R, Cowan T E, Schramm U and Bussmann M 2019 Circumventing the dephasing and depletion limits of laser-wakefield acceleration *Phys. Rev.* X **9** 031044
[6] Palastro J P, Shaw J L, Franke P, Ramsey D, Simpson T T and Froula D H 2020 Dephasingless laser wakefield acceleration *Phys. Rev. Lett.* **124** 134802

[7] Hooker S M 2013 Developments in laser-driven plasma accelerators *Nat. Photon.* **7** 775
[8] Li W-T, Wang W-T, Liu J-S, Wang C, Zhang Z-J, Qi R, Yu C-H, Li R-X and Xu Z-Z 2015 Developments in laser wakefield accelerators: from single-stage to two-stage *Chin. Phys.* B **24** 015205
[9] Joshi C 2019 Plasma-based accelerators: then and now *Plasma Phys. Control. Fusion* **61** 104001
[10] Tajima T, Yan X Q and Ebisuzaki T 2020 Wakefield acceleration *Rev. Mod. Plasma Phys.* **4** 7
[11] Leemans W P, Nagler B, Gonsalves A J, Tóth C, Nakamura K, Geddes C G R, Esarey E, Schroeder C B and Hooker S M 2006 GeV electron beams from a centimetre-scale accelerator *Nat. Phys.* **2** 696
[12] Wang X *et al* 2013 Quasi-monoenergetic laser-plasma acceleration of electrons to 2 GeV *Nat. Commun.* **4** 1988
[13] Kim H T, Pae K H, Cha H J, Kim I J, Yu T J, Sung J H, Lee S K, Jeong T M and Lee J 2013 Enhancement of electron energy to the multi-GeV regime by a dual-stage laser-wakefield accelerator pumped by petawatt laser pulses *Phys. Rev. Lett.* **111** 165002
[14] Leemans W P *et al* 2014 Multi-GeV electron beams from capillary-discharge-guided subpetawatt laser pulses in the self-trapping regime *Phys. Rev. Lett.* **113** 245002
[15] Gonsalves A J *et al* 2019 Petawatt laser guiding and electron beam acceleration to 8 GeV in a laser-heated capillary discharge waveguide *Phys. Rev. Lett.* **122** 084801
[16] Liu J S *et al* 2011 All-optical cascaded laser wakefield accelerator using ionization-induced injection *Phys. Rev. Lett.* **107** 035001
[17] Plateau G R *et al* 2012 Low-emittance electron bunches from a laser-plasma accelerator measured using single-shot x-ray spectroscopy *Phys. Rev. Lett.* **109** 064802
[18] Buck A *et al* 2013 Shock-front injector for high-quality laser-plasma acceleration *Phys. Rev. Lett.* **110** 185006
[19] Wang W T *et al* 2016 High-brightness high-energy electron beams from a laser wakefield accelerator via energy chirp control *Phys. Rev. Lett.* **117** 124801
[20] Qin Z *et al* 2018 Ultralow-emittance measurement of high-quality electron beams from a laser wakefield accelerator *Phys. Plasmas* **25** 023106
[21] Maier A R *et al* 2020 Decoding sources of energy variability in a laser-plasma accelerator *Phys. Rev.* X **10** 031039
[22] Ke L T *et al* 2021 Near-GeV electron beams at a few per-mille level from a laser wakefield accelerator via density-tailored plasma *Phys. Rev. Lett.* **126** 214801
[23] Kneip S *et al* 2010 Bright spatially coherent synchrotron x-rays from a table-top source *Nat. Phys.* **6** 980
[24] Ta Phuoc K, Corde S, Thaury C, Malka V, Tafzi A, Goddet J P, Shah R C, Sebban S and Rousse A 2012 All-optical Compton gamma-ray source *Nat. Photon.* **6** 308
[25] Corde S, Ta Phuoc K, Lambert G, Fitour R, Malka V, Rousse A, Beck A and Lefebvre E 2013 Femtosecond x rays from laser-plasma accelerators *Rev. Mod. Phys.* **85** 1
[26] Albert F and Thomas A G R 2016 Applications of laser wakefield accelerator-based light sources *Plasma Phys. Control. Fusion* **58** 103001
[27] Kozlova M *et al* 2020 Hard x rays from laser-wakefield accelerators in density tailored plasmas *Phys. Rev.* X **10** 011061
[28] Wang W *et al* 2021 Free-electron lasing at 27 nanometres based on a laser wakefield accelerator *Nature* **595** 516
[29] Kim H T *et al* 2017 Stable multi-GeV electron accelerator driven by waveform-controlled PW laser pulses *Sci. Rep.* **7** 10203
[30] Lu W, Tzoufras M, Joshi C, Tsung F S, Mori W B, Vieira J, Fonseca R A and Silva L O 2007 Generating multi-GeV electron bunches using single stage laser wakefield acceleration in a 3D nonlinear regime *Phys. Rev. Spec. Top. Accel. Beams* **10** 061301
[31] Zhang Z *et al* 2015 Generation of high quality electron beams from a quasi-phase-stable cascaded laser wakefield accelerator with density-tailored plasma segments *New J. Phys.* **17** 103011
[32] Gonsalves A J, Rowlands-Rees T P, Broks B H P, van der Mullen J J A M and Hooker S M 2007 Transverse interferometry of a hydrogen-filled capillary discharge waveguide *Phys. Rev. Lett.* **98** 025002
[33] Daniels J, van Tilborg J, Gonsalves A J, Schroeder C B, Benedetti C, Esarey E and Leemans W P 2015 Plasma density diagnostic for capillary-discharge based plasma channels *Phys. Plasmas* **22** 073112
[34] Gonsalves A J *et al* 2016 Demonstration of a high repetition rate capillary discharge waveguide *J. Appl. Phys.* **119** 033302
[35] Kameshima T *et al* 2009 Laser pulse guiding and electron acceleration in the ablative capillary discharge plasma *Phys. Plasmas* **16** 093101
[36] McGuffey C *et al* 2009 Guiding of 35 TW laser pulses in ablative capillary discharge waveguides *Phys. Plasmas* **16** 113105
[37] Qin Z *et al* 2018 Hybrid capillary discharge waveguide for laser wakefield acceleration *Phys. Plasmas* **25** 073102
[38] Takashi K *et al* 2008 0.56 GeV laser electron acceleration in ablative-capillary-discharge plasma channel *Appl. Phys. Express* **1** 066001
[39] Lu H Y *et al* 2011 Laser wakefield acceleration of electron beams beyond 1 GeV from an ablative capillary discharge waveguide *Appl. Phys. Lett.* **99** 091502
[40] Spence D J and Hooker S M 2000 Investigation of a hydrogen plasma waveguide *Phys. Rev.* E **63** 015401
[41] Bobrova N A, Esaulov A A, Sakai J I, Sasorov P V, Spence D J, Butler A, Hooker S M and Bulanov S V 2001 Simulations of a hydrogen-filled capillary discharge waveguide *Phys. Rev.* E **65** 016407
[42] Levin M *et al* 2006 Long plasma channels in segmented capillary discharges *Phys. Plasmas* **13** 083108
[43] Turner M *et al* 2021 Radial density profile and stability of capillary discharge plasma waveguides of lengths up to 40 cm *High Power Laser Sci. Eng.* **9** e17
[44] Miller H C 1993 Flashover of insulators in vacuum: review of the phenomena and techniques to improved holdoff voltage *IEEE Trans. Electr. Insul.* **28** 16
[45] Luo J *et al* 2018 Multistage coupling of laser-wakefield accelerators with curved plasma channels *Phys. Rev. Lett.* **120** 154801
[46] Tanaka K A, Yabuuchi T, Sato T, Kodama R, Kitagawa Y, Takahashi T, Ikeda T, Honda Y and Okuda S 2005 Calibration of imaging plate for high energy electron spectrometer *Rev. Sci. Instrum.* **76** 013507
[47] Qin Z *et al* 2018 Optimization of gas-filled quartz capillary discharge waveguide for high-energy laser wakefield acceleration *Phys. Plasmas* **25** 043117
[48] Jang D G, Kim M S, Nam I H, Uhm H S and Suk H 2011 Density evolution measurement of hydrogen plasma in capillary discharge by spectroscopy and interferometry methods *Appl. Phys. Lett.* **99** 141502
[49] Bagdasarov G A *et al* 2017 Laser beam coupling with capillary discharge plasma for laser wakefield acceleration applications *Phys. Plasmas* **24** 083109
[50] Garland J M *et al* 2021 Combining laser interferometry and plasma spectroscopy for spatially resolved high-sensitivity plasma density measurements in discharge capillaries *Rev. Sci. Instrum.* **92** 013505
[51] Yan W *et al* 2014 Concurrence of monoenergetic electron beams and bright x-rays from an evolving laser-plasma bubble *Proc. Natl. Acad. Sci. USA* **111** 5825

[52] Zeng M, Chen M, Sheng Z-M, Mori W B and Zhang J 2014 Self-truncated ionization injection and consequent monoenergetic electron bunches in laser wakefield acceleration *Phys. Plasmas* **21** 030701
[53] Mirzaie M *et al* 2015 Demonstration of self-truncated ionization injection for GeV electron beams *Sci. Rep.* **5** 14659
[54] Sahai A A 2019 Strongly mismatched regime of nonlinear laser-plasma acceleration: optimization of laser-to-energetic particle efficiency *IEEE Trans. Plasma Sci.* **47** 2847
[55] Lehe R, Kirchen M, Andriyash I A, Godfrey B B and Vay J-L 2016 A spectral, quasi-cylindrical and dispersion-free particle-in-cell algorithm *Comput. Phys. Commun.* **203** 66
[56] Kirchen M, Lehe R, Godfrey B B, Dornmair I, Jalas S, Peters K, Vay J-L and Maier A R 2016 Stable discrete representation of relativistically drifting plasmas *Phys. Plasmas* **23** 100704
[57] Rovige L *et al* 2020 Demonstration of stable long-term operation of a kilohertz laser-plasma accelerator *Phys. Rev. Spec. Top. Accel. Beams* **23** 093401
[58] Rowlands-Rees T P *et al* 2008 Laser-driven acceleration of electrons in a partially ionized plasma channel *Phys. Rev. Lett.* **100** 105005